Itinerant magnetic phases and quantum Lifshitz transitions in a three-dimensional repulsively interacting Fermi gas with spin-orbit coupling

Shang-Shun Zhang,[1,2,3] Jinwu Ye,[1,2,4] and Wu-Ming Liu[3]

[1]*Department of Physics, Capital Normal University, Key Laboratory of Terahertz Optoelectronics, Ministry of Education, and Beijing Advanced innovation Center for Imaging Technology, Beijing, 100048, China*

[2]*Department of Physics and Astronomy, Mississippi State University, Mississippi 39762, USA*

[3]*Beijing National Laboratory for Condensed Matter Physics, Institute of Physics, Chinese Academy of Sciences, Beijing 100190, China*

[4]*Kavli Institute of Theoretical Physics, University of California, Santa Barbara, Santa Barbara, California 93106, USA*

(Received 9 August 2015; revised manuscript received 6 July 2016; published 9 September 2016)

Magnetic phenomena in itinerant electron systems have been at the forefront of materials science. Here we show that the Weyl spin-orbit coupling (SOC) in three-dimensional repulsively interacting itinerant Fermi systems opens up a platform to host new itinerant magnetic phases, excitations, and phase transitions. A putative ferromagnetic state (FM) is always unstable against a stripe spiral spin density wave (S-SDW) or a stripe longitudinal SDW (LSDW) at small or large SOC strengths, respectively. The stripe-ordering wave vector is given by the nesting momentum of the two SOC-split Fermi surfaces with the same or opposite helicities at small or large SOC strengths, respectively. The LSDW is accompanied by a charge density wave (CDW) with half of its pitch. The transition from the paramagnet to the SSDW or LSDW+CDW is described by quantum Lifshitz-type actions, in sharp contrast to the Hertz-Millis types for itinerant electron systems without SOC. The collective excitations and Fermi surface reconstructions inside the SSDW and LSDW+CDW are also studied. The effects of a harmonic trap in cold-atom experiments are briefly discussed. In view of recent ground-breaking experimental advances in generating two-dimensional SOC in cold atoms, these phenomena can be observed in current or near-future cold-atom experiments even at very weak interactions. They may also be relevant to some itinerant magnetic materials with a strong SOC.

DOI: 10.1103/PhysRevB.94.115121

I. INTRODUCTION

The investigation and control of spin-orbit coupling (SOC) [1] have become subjects of intensive research in condensed matter and cold atoms since the discovery of the topological insulators [2,3]. It was found to be a critical factor leading to a whole new class of electronic states in correlated electron materials [4]. In cold-atom systems, since the experimental realizations of one-dimensional (1d) SOC 6 years ago [5,6], there have been recent ground-breaking experimental advances in generating 2d Rashba SOC in both ^{40}K Fermi gas [7–9] and ^{87}Rb spinor BECs [10]. The possible heating issues in these experiments are well under control, and many-body phenomena due to the interplay between SOC and interactions are being investigated. Generating the 2d SOC is a tremendous advance over the 1d SOC generated in previous experiments (for a review, see [5]), while generalizing 2d SOC to 3d SOC in these experiments is straightforward. So the 3d isotropic (Weyl) SOC is expected to be implemented in very near future experiments. So far, there have been extensive theoretical investigations on various effects of SOC on the pairing physics of attractively interacting Fermi gases [11,12]. However, there are still relatively few works on the repulsive side. In view of the tunability of weak to strong repulsive interaction in the current experiments [7–10], it becomes topical and important to investigate possible new many-body phenomena due to the interplay between the SOC and the repulsive interactions [13–18].

On the other forefront, magnetic phases and phase transitions in itinerant electron systems has been a vigorous research field in materials science. It dates back to Stoner's ferromagnetic (FM) instability [19], Hertz-Millis theory [20,21] to describe magnetic transition in itinerant Fermi systems without SOC, up to recent doping-dependent charge and spin orderings in high-temperature superconductors [22,23]. In cold-atom systems, there has been both experimental [24] and theoretical work [25] on possible itinerant FM in a purely repulsively interacting two-component Fermi system. But so far, possible dramatic effects of the SOC on the magnetic orders and transitions in the itinerant fermionic systems have not been discussed.

In this paper, we address this outstanding problem by studying repulsively interacting Fermi gas with the Weyl SOC. We show that the SOC leads to new classes of itinerant magnetic phases, excitations, and phase transitions. We classify the symmetries of the SOC Hamiltonian and find their exact constraints on the density-spin response functions. On the paramagnet (PM) side, we identify one gapless mode and three gapped modes (one longitudinal and two transverse modes). The SOC leads to the splitting of two transverse modes at any finite momentum. A putative ferromagnetic state (FM) is always unstable against a stripe coplanar spiral spin density wave (S-SDW) or a stripe collinear longitudinal SDW (LSDW) at small or large SOC strengths, respectively. Their stripe-ordering wave vector is given by the nesting momentum of the two Fermi surfaces split by the SOC with the same helicity or opposite helicities at small or large SOC strengths, respectively. There is an accompanying charge density wave (CDW) to the LSDW with half of its pitch. We also construct a unified quantum Ginzburg-Landau action to study the PM to the putative FM, SSDW, or LSDW+CDW transition and find it is of quantum Lifshitz type which is in sharp contrast to Hertz-Millis type for itinerant electron systems

without SOC. The collective excitations and Fermi surface (FS) reconstructions inside the SSDW and LSDW+CDW are also studied. At a relatively large SOC (or dilute Fermi gas), even a very weak interaction can drive the system into the SSDW or LSDW+CDW due to the nearly flat band structure near the bottom (Weyl shell) of the spectrum. This salient feature makes these novel itinerant magnetic phases easily experimentally accessible even at weak interactions. Near the end of the paper, we briefly discuss the effects of the harmonic trap in observing these phenomena. In view of recent ground-breaking experimental realizations of a 2d SOC [7–10], these new phenomena could be probed [5,26–31] in near-future cold-atom experiments and may also be relevant to some materials with SOC [4,17].

The Hamiltonian for a repulsively interacting two-component Fermi gas with the isotropic Weyl SOC $V_{SO} = \lambda\vec{k}\cdot\vec{\sigma}$ is

$$H = \int d^3\vec{r}\Big[\Psi^\dagger\Big(\frac{-\hbar^2\nabla^2}{2m} - \mu + V_{SO}\Big)\Psi + g\int d^3\vec{r}\Psi^\dagger_\uparrow(\vec{r})\Psi^\dagger_\downarrow(\vec{r})\Psi_\downarrow(\vec{r})\Psi_\uparrow(\vec{r})\Big], \quad (1)$$

where the SOC strength $\lambda = \frac{g_F\mu_B\nabla B}{3m\hbar}$ can be tuned by the magnetic field gradient ∇B in the scheme [32,33], g_F is the Landé factor, μ_B is the Bohr magneton, and $g = 4\pi\hbar^2 a_s/m$ with a_s the s-wave scattering length. The chemical potential μ is determined by the density of atoms. In the cold-atom experiments [7–10], the density is fixed, so it is convenient to take $k_R = m\lambda$ as the momentum unit and $E_R = k_R^2/2m$ as the energy unit. We characterize the SOC strength by the dimensionless ratio $\gamma = k_R/k_F$ where $k_F = (6\pi^2 n)^{1/3}$ is the Fermi momentum of the system without SOC at the same density n. We set $\hbar = k_B = 1$.

The rest of the paper is organized as follows. Before performing any analytical or numerical calculations, it is important to investigate the symmetries of the Hamiltonian and find their exact constraints on experimentally observable physical quantities. This will be achieved in Sec. II. In Sec. III, we will calculate the collective modes and the particle-hole (P-H) excitations in the paramagnet state. There is one gapless density-longitudinal spin mode, one gapped density-longitudinal spin mode, and two gapped transverse modes. We also analyze why it is the SOC which leads to the splittings of the two transverse modes at any nonzero wave vector. The lower branch of the two split transverse modes indicates a transition into a transverse spiral spin density wave (SSDW) as the interaction strength increases. In Sec. IV, assuming the ferromagnetic (FM) state is a possible ground state when the interaction is above a critical strength, we construct a Hertz-Millis-type action to describe the transition from the paramagnet to the putative FM state. However, we identify a nonpositive definite transverse propagator which indicates that the putative FM state is always pre-emptied by a transverse SSDW. Then in Sec. V, we construct an effective action to describe the paramagnet to the SSDW at a small SOC and show that the transition is of bosonic quantum Lifshitz type with the instability happening at a finite momentum [34,35]. So it is a first-order one, in sharp contrast to the second-order one in itinerant Fermi systems without SOC. This maybe the first quantum Lifshitz transition in any *itinerant* Fermi system. Similar types of bosonic Lifshitz transitions exist in various condensed matter systems such as the superfluid ^{4}He [38], exciton superfluids in bilayer quantum Hall or electron-hole bilayers [39], and superconductors in a Zeeman field [36,40]. We analyze the symmetry-breaking pattern of the SSDW and work out its one gapless spin-lattice coupled Goldstone mode. In Sec. VI, we construct the quantum Lifshitz-type action to describe the paramagnet to the LSDW at a large SOC and show that there is always an accompanying charge density wave with half of its pitch. We analyze the symmetry-breaking pattern of the LSDW+CDW and work out its one gapless lattice phonon mode. Combining the results achieved in Secs. IV–VI, we reach the zero-temperature phase diagram in the interaction versus the SOC strength and also the finite-temperature phase diagrams in the SSDW and LSDW+CDW phase. In Sec. VII, we show that it is the FS nestings at a small and large SOC with the opposite or the same helicities which lead to the SSDW and LSDW+CDW at a small and large SOC, respectively. This is in sharp contrast to continuous itinerant Fermi systems without SOC where there are no FS nestings at 3d, so the FM becomes a valid instability. In Sec. VIII, we work out the corresponding FS reconstructions inside the SSDW and LSDW+CDW and also stress their different structures within the Brillouin zone (BZ). In the final conclusion, Sec. IX, we contrast the results achieved in the continuum with those on lattice systems at a half filling. We also argue that the dominant roles played by the SOC may make the magnetic transitions in itinerant Fermi systems with the SOC simpler than its counterpart without it. We discuss the experimental detections of the itinerant magnetic phases and phase transitions in the cold-atom systems and also briefly outline the effects of a harmonic trap. The novel phenomena may also be observed in some itinerant magnetic materials with a strong SOC. Several technical details are left to the three Appendices.

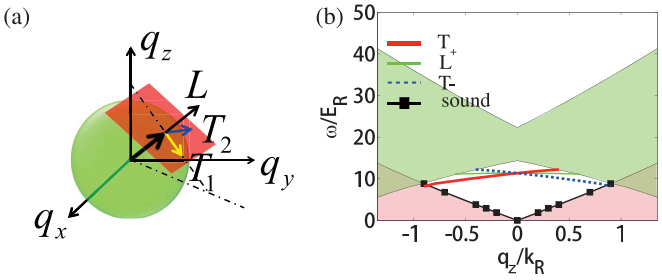

FIG. 1. (a) The helicity basis shows one longitudinal mode along the $\hat{q} = \frac{\vec{q}}{q}$ direction and two transverse modes along the two transverse directions $\hat{T}_1, \hat{T}_2$. (b) The collective modes in the normal state at $\gamma = 0.21$. The pink (green) regime represents the intraband (interband) particle-hole excitation. The split $T_\pm$ modes indicate possible SSDW at $\vec{q} = \pm Q_T\hat{z}$.

II. SYMMETRY ANALYSIS OF THE SOC HAMILTONIAN AND EXACT RELATIONS OF DENSITY-SPIN SUSCEPTIBILITIES

In the presence of Weyl SOC, it is convenient to define a helical basis [Fig. 1(a)] with respect to the momentum where

we can define two transverse spin modes ($\hat{T}_1\cdot\vec{S}$, $\hat{T}_2\cdot\vec{S}$) and one longitudinal L spin mode ($\hat{q}\cdot\vec{S}$). The Hamiltonian Eq. (1) has the following symmetries: (1) the translational symmetry and the $[\mathrm{SU}(2)_{\mathrm{spin}}\times\mathrm{SO}(3)_{\mathrm{orbit}}]_D$ symmetry where the D means the simultaneous (diagonal) rotation in spin and orbit space; (2) time-reversal symmetry T: $Tc_{\vec{k},\uparrow}T^{-1}=c_{-\vec{k},\downarrow}$, $Tc_{\vec{k},\downarrow}T^{-1}=-c_{-\vec{k},\uparrow}$; (3) three spin-orbital-coupled reflection symmetries: (a) P_x: $\sigma_x\to\sigma_x,k_y\to-k_y,\sigma_y\to-\sigma_y,k_z\to-k_z,\sigma_z\to-\sigma_z$, (b) P_y: $\sigma_y\to\sigma_y,k_x\to-k_x,\sigma_x\to-\sigma_x,k_z\to-k_z,\sigma_z\to-\sigma_z$, (c) P_z: $\sigma_z\to\sigma_z,k_x\to-k_x,\sigma_x\to-\sigma_x,k_y\to-k_y,\sigma_y\to-\sigma_y$. The P_z symmetry is equivalent to a joint π rotation of orbital and spin around the $\hat{z}$ axis. The P_y can also be taken as P_x combined with $[\mathrm{U}(1)_{\mathrm{spin}}\times\mathrm{U}(1)_{\mathrm{orbit}}]_D$ around the $\hat{z}$ axis by an angle $\pi/2$. These symmetries can be used to establish exact relations on the spin-density correlation functions.

In the helicity basis Fig. 1(a), pick up $\vec{q}$ as the $\hat{z}$ axis, then $q_x=q_y=0,q_z>0,\vec{q}=q_z\hat{z}$ in this helicity basis. The $[\mathrm{SU}(2)_{\mathrm{spin}}\times\mathrm{SO}(3)_{\mathrm{orbit}}]_D$ symmetry along this $\hat{z}$ axis dictates that

$$R_z^T\chi^{\mu\nu}R_z=\chi^{\mu\nu}, \tag{2}$$

which dictates that the dynamical 4×4 density-spin response function $\chi^{\mu\nu}(\vec{q},\omega)$ can be split into two 2×2 subspaces: (i) the density-longitudinal n-L subspace, (ii) the two transverse T_1-T_2 subspace with $\chi^{xx}=\chi^{yy},\chi^{xy}=-\chi^{yx}$.

A. In the T_1-T_2 subspace

After a unitary transformation, it can be shown that in the T_1-T_2 subspace,

$$\chi=\begin{pmatrix}\chi^{+-} & 0\\ 0 & \chi^{-+}\end{pmatrix}, \tag{3}$$

where $\chi^{+-}=2(\chi^{xx}-i\chi^{xy}),\chi^{-+}=2(\chi^{xx}+i\chi^{xy})$, $\chi^{++}=\chi^{--}=0$.

The P_x (or P_y) symmetry dictates

$$\chi^{+-}(\vec{q},\omega)=\chi^{-+}(-\vec{q},\omega). \tag{4}$$

The T symmetry also leads to Eq. (4). Equation (4) leads to $\chi^{xx}=\chi^{yy}$ as an even function of q_z, $\chi^{xy}=-\chi^{yx}$ as an odd function of q_z.

Directly taking the complex conjugate leads to

$$[\chi^{+-}(\vec{q},\omega)]^*=\chi^{-+}(-\vec{q},-\omega), \tag{5}$$

which, combining with Eq. (4), leads to

$$\begin{aligned}\mathrm{Re}\,\chi^{+-}(\vec{q},\omega)&=\mathrm{Re}\,\chi^{+-}(\vec{q},-\omega),\\ \mathrm{Im}\,\chi^{+-}(\vec{q},\omega)&=-\mathrm{Im}\,\chi^{+-}(\vec{q},-\omega).\end{aligned} \tag{6}$$

(a) *Outside the particle-hole (P-H) continuum.* The χ^{+-},χ^{-+} are real, so Eq. (6) leads to the fact that $\chi^{xx}=\chi^{yy}$ and $\chi^{xy}=-\chi^{yx}$ are all even function of ω. The poles of χ^{+-},χ^{-+} lead to the two gapped transverse modes $T_\pm$, respectively.

(b) *Inside the P-H continuum.* The χ^{+-},χ^{-+} have both real and imaginary parts. Equation (6) leads to $\mathrm{Re}\,\chi^{+-}(\vec{q},\omega)$ as an even function of ω, while $\mathrm{Im}\,\chi^{+-}(\vec{q},\omega)$ as an odd function of ω. $\mathrm{Im}\,\chi^{+-}(\vec{q},\omega)\neq0$ leads to the particle hole excitation spectrum in the T_1-T_2 subspace.

B. In the n-L subspace

The P_x (or P_y) symmetry dictates

$$\begin{aligned}\chi^{ii}(\vec{q},\omega)&=\chi^{ii}(-\vec{q},\omega),\quad i=n,L,\\ \chi^{ij}(\vec{q},\omega)&=-\chi^{ij}(-\vec{q}),\quad i\neq j,\end{aligned} \tag{7}$$

which shows χ^{nn},χ^{LL} are even functions of q_z, while χ^{nL},χ^{nL} are odd functions of q_z.

The T symmetry leads to

$$\begin{aligned}\chi^{ii}(\vec{q},\omega)&=\chi^{ii}(-\vec{q},\omega),\quad i=n,L,\\ \chi^{ij}(\vec{q},\omega)&=-\chi^{ji}(-\vec{q},\omega),\quad i\neq j.\end{aligned} \tag{8}$$

Note that P_x and T leads to two different equations in the nL component only. Combining Eq. (7) and Eq. (8) leads to $\chi^{nL}(\vec{q},\omega)=\chi^{Ln}(\vec{q},\omega)$.

Directly taking the complex conjugate leads to

$$[\chi^{ij}(\vec{q},\omega)]^*=\chi^{ij}(-\vec{q},-\omega),\quad i,j=n,L, \tag{9}$$

which combining with Eq. (7) leads to

$$\begin{aligned}\mathrm{Re}\,\chi^{ii}(\vec{q},\omega)&=\mathrm{Re}\,\chi^{ii}(\vec{q},-\omega),\quad i=n,L,\\ \mathrm{Im}\,\chi^{ii}(\vec{q},\omega)&=-\mathrm{Im}\,\chi^{ii}(\vec{q},-\omega),\end{aligned} \tag{10}$$

and

$$\begin{aligned}\mathrm{Re}\,\chi^{nL}(\vec{q},\omega)&=-\mathrm{Re}\,\chi^{nL}(\vec{q},-\omega),\\ \mathrm{Im}\,\chi^{nL}(\vec{q},\omega)&=\mathrm{Im}\,\chi^{nL}(\vec{q},-\omega).\end{aligned} \tag{11}$$

(a) *Outside the P-H continuum.* The $\chi^{nn},\chi^{LL},\chi^{nL}$ are real. Equation (10) leads to $\chi^{nn}(\vec{q},\omega),\chi^{LL}(\vec{q},\omega)$ as even functions of ω. However, Eq. (11) leads to $\chi^{nL}(\vec{q},\omega)$ as an odd function of ω, therefore $\chi^{nL}(\vec{q},0)=0$. The poles of the 2×2 matrix determinant lead to one gapless sound mode and a gapped L mode.

(b) *Inside the P-H continuum.* The $\chi^{nn},\chi^{LL},\chi^{nL}$ have both real and imaginary parts. Equations (10) and (11) lead to $\mathrm{Re}\,\chi^{ii}(\vec{q},\omega)$, $i=n,L$ [$\mathrm{Re}\,\chi^{nL}(\vec{q},\omega)$] as an even [odd] function of ω, while $\mathrm{Im}\,\chi^{ii}(\vec{q},\omega)$ [$\mathrm{Im}\,\chi^{nL}(\vec{q},\omega)$] is an odd [even] function of ω. $\mathrm{Im}\,\chi^{nL}(\vec{q},\omega)\neq0$ leads to the particle-hole excitation spectrum in the n-L subspace.

These exact relations can be used to simplify considerably the following analytical and numerical calculations to find the 4 collective modes and the P-H excitations. Any approximations such as the random phase approximation (RPA) should respect these exact relations.

III. COLLECTIVE MODES AND THE P-H EXCITATIONS IN THE PARAMAGNET STATE

In this section, we will perform a concrete calculation on all the response functions at the RPA level whose poles lead to the collective modes. We also ensure that they all satisfy the exact relations established in the last section.

The interaction term in Eq. (1) can be divided into the density and spin channel $\mathcal{H}_I=\frac{g}{8}\int d\vec{r}[\rho(\vec{r})^2-\vec{S}(\vec{r})^2]$, where $\rho(\vec{r})=\Psi^\dagger\Psi(\vec{r})$ and $\vec{S}(\vec{r})=\Psi^\dagger\vec{\sigma}\Psi(\vec{r})$. In the presence of SOC, the density fluctuation is coupled with the spin fluctuation [14]. We introduce the density-spin order parameter $\phi_\mu,\mu=n,x,y,z$ to decouple the interaction term via a Hubbard-Stratonovich transformation. Integrating out the fermionic

fields leads to the effective action for ϕ_μ:

$$\mathcal{S} = \int d^3\vec{r} \int_0^{1/T} d\tau \frac{1}{2g}\phi_\mu^2 - \mathrm{Tr}\ln\left(-\mathcal{G}_0^{-1} + M\right), \quad (12)$$

where $\mathcal{G}_0^{-1} = -\partial_\tau - \mathcal{H}_0 + \mu$, $M = \frac{i}{2}\phi_n\sigma^0 + \frac{1}{2}\vec{\phi}\cdot\vec{\sigma}$.

Now we can expand Eq. (12) $\mathcal{S}[\phi_\mu] = \mathcal{S}^{(0)} + \mathcal{S}^{(2)} + \cdots$ in terms of ϕ_μ. The density channel ϕ_n has a nonzero imaginary saddle-point value due to the finite particle density of the fermions which could be eliminated by redefining ϕ_n as the deviation from its saddle-point value. To the second order of ϕ_μ, we obtain

$$\mathcal{S}^{(2)} = \frac{1}{2}\int \frac{d^3\vec{k}}{(2\pi)^3} T\sum_n \left(\frac{1}{g}\delta^{\mu\nu} - \frac{1}{4}\bar{\chi}^{\mu\nu}(\vec{k}, i\omega_n)\right) \times \phi^\mu(\vec{k}, i\omega_n)\phi^\nu(-\vec{k}, -i\omega_n), \quad (13)$$

where $\bar{\chi}^{\mu\nu}$ is related to the density-spin susceptibility $\chi^{\mu\nu}(\mathbf{q}, i\omega_n) = \langle s^\mu(\mathbf{q}, i\omega_n)s^\nu(-\mathbf{q}, -i\omega_n)\rangle$ via $\bar{\chi}^{00} = -\chi^{00}$, $\bar{\chi}^{0i} = i\chi^{0i}$, $\bar{\chi}^{i0} = i\chi^{i0}$, $\bar{\chi}^{ij} = \chi^{ij}$, with $i,j = x,y,z$. The noninteracting density-spin susceptibility is given by

$$\chi_0^{\mu\nu}(\vec{q}, i\omega_n) = \frac{1}{V}\sum_{k,sr} F_{sr}^{\mu\nu}(k+q,k)\frac{n_F(\xi_{k+q,s}) - n_F(\xi_{k,r})}{i\omega_n - (\xi_{k+q,s} - \xi_{k,r})}, \quad (14)$$

where $\xi_{k,s}$ is the fermion spectrum with s the helicity $\hat{p}\cdot\vec{\sigma}|ps\rangle = s|ps\rangle$; $n_F(\xi_{k,s})$ is the Fermi distribution function; $\xi_{k+q,s} - \xi_{k,r}$ is the particle-hole excitation energy; and the overlap factor $F_{sr}^{\mu\nu}(p,q) = \langle ps|\sigma^\mu|qr\rangle\langle qr|\sigma^\nu|ps\rangle$.

We check that Eq. (13) satisfies all the exact relations derived in the last section. One can extract collective modes through the poles of density-spin response functions at the RPA level. In the n-L subspace, the mixing of density and longitudinal modes leads to one gapless sound (black) mode $\omega_q^s = v_s q$ and one gapped (called L) (green) mode $\omega_L(\vec{q}) = \Delta + \alpha q^2$ where $\alpha < 0$ in Fig. 1(b). In the T_1-T_2 subspace, there are two split transverse modes $\omega_{T_{+/-}}(\vec{q}) = \Delta \pm \beta q_z$ in Fig. 1(b). The T_+ mode (red) is the pole of χ^{+-}, while T_- (blue) is the pole of χ^{-+}. The exact symmetry Eq. (3) indicates T_+ and T_- exchanges under $q_z \to -q_z$. The restored $\mathrm{SU}(2)_{\mathrm{spin}}$ symmetry at $\vec{q} = 0$ dictates that the three gapped modes must have the same gap Δ at $q = 0$. The level repulsion in the n-L space pushes the sound mode quite close to the intraband P-H continuum [Fig. 1(b)]. Similarly, the level repulsion in the (T_1, T_2) space will also split the two transverse modes $T_\pm$. So at finite but small q, the three modes split with the order $\omega_{T_+} > \omega_L > \omega_{T_-}$.

In principle, $\mathrm{Im}\,\chi^{+-}(\vec{q},\omega) \neq 0$ need not to happen at the same time as $\mathrm{Im}\,\chi^{nL}(\vec{q},\omega) \neq 0$. However, at the RPA level Eq. (14) employed here, they happen at the same time. So the P-H excitation spectrum in the (T_1, T_2) space is the same as that in (n, L) space at the RPA level. Very similarly, the P-H excitation spectrum in the density channel is the same as that in the spin channel at the RPA level in the conventional Fermi gas discussed in Appendix A 2.

We find that Δ vanishes when $g > g_s = 24\pi^2 k_R/m(k_{F2}^2 - k_{F1}^2)$, where $k_{F2} > k_{F1}$ are the two Fermi momenta split due to the SOC. This corresponds to an instability driven by the collective modes at $q = 0$. However, Fig. 1(b) indicates that $\omega_{T_{+/-}}(\vec{q}) = \Delta \pm \beta q_z$ may become negative simultaneously at $\pm Q_T\hat{z}$ before $\Delta = 0$ at $q = 0$. This indicates a transverse (spiral, chiral, and coplanar) SDW transition at $\pm Q_T\hat{z}$ with the order parameter $\vec{\phi}_T = \phi_0(\cos Qz, \sin Qz, 0)$. Such an instability is confirmed further in the P-H channel to be discussed in the following section.

The mechanism for why T_+ and T_- splits

In fact, in order to guarantee the two T_+, T_- modes to be degenerate, one need to have both T symmetry and the inversion symmetry I: $\vec{q} \to -\vec{q}$. The I symmetry dictates that

$$\chi^{+-}(\vec{q},\omega) = \chi^{+-}(-\vec{q},\omega), \chi^{-+}(\vec{q},\omega) = \chi^{-+}(-\vec{q},\omega). \quad (15)$$

Combining Eq. (4) with Eq. (15) leads to

$$\chi^{+-}(\vec{q},\omega) = \chi^{-+}(\vec{q},\omega). \quad (16)$$

Alternatively, if assuming S_x symmetry, $\sigma_x \to \sigma_x, \sigma_{y,z} \to -\sigma_{y,z}$, one also find Eq. (16). Here, it is the SOC which breaks the inversion symmetry, so $\chi^{+-}(\vec{q},\omega) \neq \chi^{-+}(\vec{q},\omega)$ for $\vec{q} \neq 0$ which leads to the splitting of the two transverse modes even in the normal phase at any $\vec{q} \neq 0$. Only at $\vec{q} = 0$, the SOC vanishes, and the three modes have the same gap.

Similar mechanisms happens in the 3d Dirac fermions [4]. If keeping both the TR and inversion symmetry, one gets the 4-component Dirac fermions. When breaking only one of the two symmetries, the 4-component Dirac fermion splits into 2 two-component Weyl fermions. The splitting in the bulk also generates the corresponding Fermi-arc states on the 2d surfaces.

IV. INSTABILITY OF THE FERROMAGNETIC STATE

There is a Stoner FM instability when $\delta = \frac{1}{g_c} - \frac{\chi_0}{4} = 0$, where $\chi_0(\vec{q} \to 0, \omega = 0) = \frac{m}{6\pi^2}(\frac{k_{F1}^2 + k_{F2}^2}{K} + \frac{k_{F2}^2 - k_{F1}^2}{k_R}), K = \sqrt{k_R^2 + 2m\mu}$ is the static spin susceptibility of 3d noninteracting Fermi gas with the Weyl SOC. We obtain the critical value of dimensionless interaction strength $k_F a_s^c$ (black dashed line) shown in Fig. 2(a). As γ increases, $F(\gamma)$ has a maximum at $\gamma \simeq 0.63$ corresponding to the chemical potential $\mu \sim 0$, after which, $k_F a_s^c$ decreases quickly. At a strong SOC, the μ approaches the bottom of the spectrum (the Weyl shell at $|\vec{k}| = k_R$), where the density of states diverges as $\frac{1}{\sqrt{\epsilon}}$ [see Fig. 7(a)]. The effects of an interaction are dramatically enhanced; even a weak interaction may drive the system into the putative itinerant FM state. Indeed, in the strong SOC limit $\mu \to -1$, the critical interaction strength to reach the putative FM $g_c = 12\pi^2\sqrt{1+\mu} + O((1+\mu)^{3/2})$ reduces to zero. Because $g_c < g_s$ calculated in the last section, the FM instability happens before that driven by the $q = 0$ instability of the collective modes.

Following Hertz-Millis [20,21] to study the FM onset transition in itinerant Fermi systems without SOC, taking the $\vec{q} \to 0, \omega/v_F q \to 0$ limit and integrating out the noncritical density mode, we obtain the effective action in terms of the spin fluctuation order parameters $\vec{\phi}$ (see Appendix B):

$$\mathcal{S} = \int \frac{d^3\vec{q}}{(2\pi)^3} T\sum_n \frac{1}{2}\mathcal{G}_s^{-1}\hat{P}_s^{ij}\phi_i\phi_j + u\int d^3\vec{r}d\tau(\vec{\phi}^2)^2, \quad (17)$$

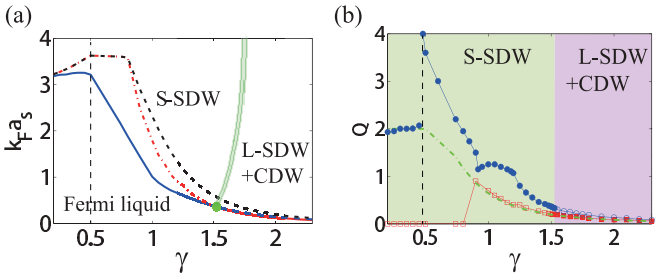

FIG. 2. The zero-temperature phase diagram achieved by the RPA calculations. (a) The critical interaction strength from the PM Fermi liquid to SSDW [blue line; Fig. 3(a)], LSDW+CDW (red dash-dotted line; Fig. 3(b)], or a putative FM (black dashed line) transition. The FM is always unstable against the SSDW. (b) The ordering wave vector Q_T (blue circles) of the SSDW and Q_L (red squares) of the LSDW as a function of SOC strength γ. The green dot-dashed line represents the $k_{F2}-k_{F1}$. When $\gamma<0.5$, $Q_T\sim k_{F2}-k_{F1}=2k_R$ is dominated by the nearly FS nesting between outer FS and inner FS with the opposite helicity. When $0.5<\gamma<1.5$, Q_T is determined by multiple momentum transfer processes. The phase in this regime could be some SSDW with multimomenta orderings. When $\gamma>1.5$, $Q_L\sim k_{F2}-k_{F1}$ is dominated by the nearly FS nesting between outer FS and inner FS with the same helicity [43]. See Fig. 3 for the spin-orbital configurations of SSDW and LSDW+CDW, Fig. 4 for the finite-temperature phase transitions, and Fig. 6 for the Fermi surface reconstructions in the SSDW and LSDW+CDW.

where $\hat{P}_s^{ij}=\hat{n}_s^i\hat{n}_s^j$ ($\hat{n}_s=\hat{T}_+,\hat{T}_-,\hat{L}$) is the projection operator into the helical basis, and $\mathcal{G}_{T_\pm}^{-1}=\delta+\gamma_T^0|y|\pm\beta_T q+\alpha_T q^2$ and $\mathcal{G}_L^{-1}=\delta+\gamma_L^0 y^2+\alpha_L q^2$, where $y=\omega_n/v_F q$ are the propagators of the helical spin modes. Note that the $SU(2)_{spin}$ symmetry at $\vec{q}=0$ dictates that there is only one tuning parameter δ from the PM to the putative FM transition. When $\delta>0$ ($\delta<0$), it is in the PM (FM) phase. However, we observe that the $\pm q$ terms in the transverse propagators are dictated by the exact symmetry Eqs. (3) and (4). They indicate that the putative FM is pre-emptied by the spiral spin density wave (SSDW) [Fig. 3(a)] at a finite q determined by the divergence of the static transverse susceptibility $\chi^{+-}(Q_T\hat{z},\omega=0)$ [41].

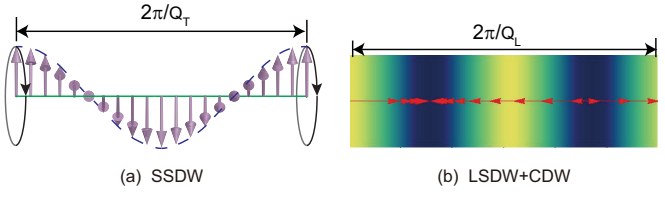

FIG. 3. The spin-orbital configurations along the stripe direction z of (a) itinerant spiral spin density wave (SSDW) with a uniform density and (b) itinerant longitudinal spin density wave (LSDW) with the accompanying charge density wave (CDW). In (b), the background with varying colors shows the CDW background induced by the LSDW order, whose spatial period is half that of the LSDW. Yellow (blue) means high (low) density. Fermionic degrees of freedom are not shown.

V. QUANTUM LIFSHITZ TRANSITION FROM THE PARAMAGNET TO SSDW TRANSITION AT A SMALL SOC

Due to the exact relation Eq. (3), one also gets the pole at $\chi^{-+}(-Q_T\hat{z},\omega=0)$ due to the T_- mode. So $\pm Q_T$ has to appear in pairs, indicating the SSDW $\langle S_+\rangle=e^{i(Q_Tz+\theta)},\langle S_-\rangle=e^{-i(Q_Tz+\theta)}$ shown in Fig. 3(a). The critical interaction strength $k_F a_s^c$ and its orbital momentum Q_T are shown in Figs. 2(a) and 2(b), respectively.

In Eq. (17), when $\gamma<1.5$, near the PM to the SSDW transition, the critical T_- propagator is given by

$$\mathcal{G}_{T_-}^{-1}=\delta_{T_-}+\gamma_T|\omega_n|+\alpha_T(q-Q_T)^2, \tag{18}$$

where $\delta_{T_-}=\delta-\frac{\beta_T^2}{4\alpha_T}$, $\gamma_T=\gamma_T^0/v_F Q_T$, $Q_T=\frac{\beta_T}{2\alpha_T}=k_{F2}-k_{F1}=2k_R$. The propagator plus the interaction u term in Eq. (17) leads to the quantum version of the classical Lifshitz type of action to describe the transition from a paramagnet state to a modulated state [34,35]. It was shown in [36] that the interaction u term favors a stripe state, which is confirmed here by the calculations at the RPA level. When $\delta_{T_-}>0$, it is in the PM state where $\langle\phi_-\rangle=0$. When $\delta_{T_-}<0$, it is in the stripe SSDW state where $\langle\phi_-\rangle=\phi_0 e^{-i(Q_Tz+\theta)}$. It is a first-order quantum Lifshitz type of transition [36–40], so the dynamic exponent z cannot be defined. This is in sharp contrast to the second-order transition with the $z=3$ (FM) or $z=2$ (AFM) in the Hertz-Millis action Eq. (B1) to describe magnetic phase transitions in itinerant electron systems without SOC.

The symmetry breaking from the PM to the SSDW is $[SU(2)_{spin}\times SO(3)_{orbit}]_D\times Tran\to[U(1)^z_{spin}\times U(1)_{orbit}]^\alpha_D\times(z\to z+\alpha/Q_T)$, where α is the rotation angle. Of course, when $\alpha=2\pi$, the order parameter gets back to itself, and it reduces to just a translation by a lattice constant $z\to z+a$. It leads to one gapless Goldstone mode θ in $\vec{\phi}_T=\phi_0(\cos(Qz+\theta),\sin(Qz+\theta),0)$. By a symmetry analysis, we get the effective action of the Goldstone mode

$$\mathcal{L}_T[\theta]=(\partial_\tau\theta)^2+a_T(\partial_z\theta)^2+b_T(\partial_\perp\theta)^2. \tag{19}$$

There is a finite-temperature 3d XY transition driven by the vortex unbinding in the phase of the Goldstone mode θ where the SSDW also melts simultaneously [Fig. 4(a)].

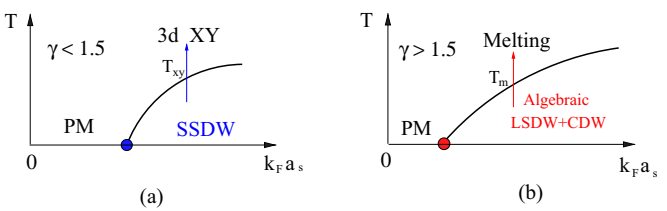

FIG. 4. Finite-temperature phase diagram of itinerant Fermi gas with Weyl SOC. Blue (red) dot stands for the first-order bosonic Lifshitz transition to the SSDW (LSDW+CDW). (a) The SSDW will survive up to a 3d XY transition temperature T_{xy} driven by the phase fluctuations. (b) Any $T>0$ will transfer the LSDW+CDW into an algebraic one which, in turn, will melt through a melting transition at T_m driven by lattice dislocations.

VI. QUANTUM LIFSHITZ TRANSITION FROM THE PARAMAGNET TO LSDW+CDW TRANSITION AT A LARGE SOC

When $\gamma > 1.5$, the chemical potential approaches the bottom of the Weyl shell, and the divergence of the static longitudinal susceptibility $\chi_{LL}(\pm Q_L\hat{z},\omega = 0)$ happens first before that of the transverse one, indicating the LSDW in Fig. 3(b): $\vec{\phi}_L = \phi_0(0,0,\cos(Q_L z + \theta))$ where the $Q_L = k_{F2} - k_{F1}$ is the FS nesting ordering wave vector to be shown in the next section. The critical interaction strength $k_F a_s^c$ and its orbital momentum Q_L are shown in Figs. 2(a) and 2(b), respectively.

In Eq. (17), near the PM to the LSDW+CDW transition, $\alpha_L < 0$ in the L propagator, so one need to expand it to the q^4 order. We also find a damping term emerges at larger momenta due to the coupling to the gapless PH excitations: $\mathcal{G}_L^{-1} = \delta + \alpha_L q^2 + u_L q^4 + \gamma_L^0 y^2 + \gamma_L^1|y| + \cdots$ where $u_L > 0$, the critical L propagator becomes:

$$\mathcal{G}_L^{-1} = \delta_L + \gamma_L|\omega_n| + u_L(q^2 - Q_L^2)^2, \tag{20}$$

where $\delta_L = \delta - \frac{\alpha_L^2}{4u_L}, \gamma_L = \gamma_L^1/v_F Q_L, Q_L = (\frac{|\alpha_L|}{2u_L})^{1/2} = k_{F2} - k_{F1}$. It was shown [36] that the interaction u term in Eq. (17) favors a stripe state, which is confirmed here by the calculations at the RPA level. When $\delta_L > 0$, it is in the PM state where $\langle\phi_L\rangle = 0$. When $\delta_L < 0$, it is in the stripe [36] LSDW state where $\langle\phi_L\rangle = \phi_0\cos(Q_L z + \theta)$. This is also a first-order quantum Lifshitz type of transition [37]. There is also a cubic coupling [42] between the charge and spin $\mathcal{S}_3 = \lambda_3\delta\phi_n\phi_L^2$ which leads to an accompanying CDW with $Q_c = 2Q_L$ inside the LSDW: $\delta\phi_n = \phi_0^2\cos(2Q_L z + 2\theta)$ inside the LSDW, consistent with the numerical calculations shown in Fig. 3(b).

The symmetry breaking from the PM to the LSDW+CDW $[\mathrm{SU}(2)_{\mathrm{spin}} \times \mathrm{SO}(3)_{\mathrm{orbit}}]_D \times \mathrm{Tran} \to [\mathrm{U}(1)^z_{\mathrm{spin}} \times \mathrm{U}(1)_{\mathrm{orbit}}]_D \times (z \to z + 2\pi/Q_L)$ leads to one gapless lattice phonon mode θ. By symmetry analysis and drawing the analogy from the smectic liquid crystal [35], we get the effective action of the lattice phonon mode:

$$\mathcal{L}_L[\theta] = (\partial_\tau\theta)^2 + a_L(\partial_z\theta)^2 + b_L(\partial_\perp^2\theta)^2. \tag{21}$$

At any finite temperatures, it becomes an algebraic ordered spin nematic state [Fig. 4(b)]; its longitudinal spin structure factor [16] shows a power-law rather than a δ-function singularity at $\vec{q} = \pm Q_L\hat{z}$:

$$S_{LL}(\vec{q} \pm Q_L\hat{z}) \sim \begin{cases} \phi_0^2(q_z \pm Q_L)^{-2+\eta_L}, & \text{if } q_\perp = 0, \\ \phi_0^2 q_\perp^{-4+2\eta_L}, & \text{if } q_z = 0, \end{cases} \tag{22}$$

where $\eta_L = \frac{T}{8\pi(a_L b_L)^{1/2}}$. There is also an associated power-law singularity for the density structure factor at $\vec{q} = \pm 2Q_L\hat{z}$.

In the $\gamma \to \infty$ limit, or equivalently the zero-density limit, the system may become a Wigner crystal. In this limit, the RPA approach, which in principle works for the high-density limit only, breaks down. A strong-coupling approach to treat the interaction nonperturbatively may be needed to work out the true ground state in such a zero-density limit.

Figure 4 is dramatically different than the corresponding phase diagrams without SOC studied by Hertz, Millis, and others [20,21] in all the physical quantities such as the quantum phases, excitations spectra, and universality classes of quantum and classical phase transitions. It is easy to see that both SSDW and LSDW+CDW carry the density current $\vec{j}_{T/L} = \lambda\vec{\phi}_{T/L}$ which is absent in the PM, putative FM, or any itinerant states without SOC. This feature maybe useful in their experimental detections.

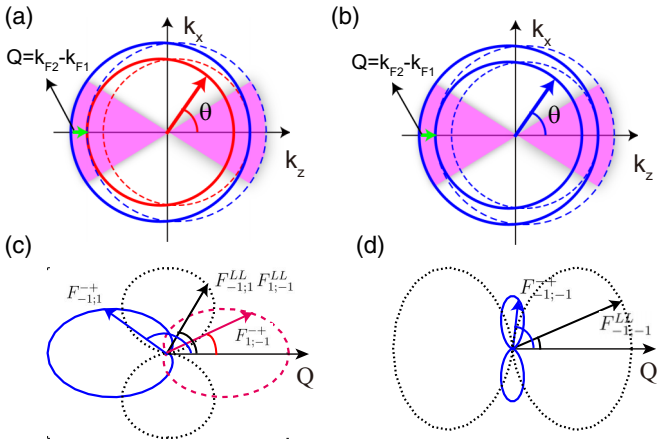

FIG. 5. Fermi surface nesting and overlap factor. (a) The Fermi surfaces shown by the solid circles for small SOC ($\gamma \ll 1$), where the two Fermi surfaces have different helicities (different colors). The dashed circles are the ones after translation with the nesting momentum $Q = k_{F2} - k_{F1} = 2k_R$ with $k_{F1,2}$ the Fermi momenta. The angle θ shows the position at the Fermi surface. The Fermi surfaces inside the shaded regime around $\theta = 0,\pi$ are well nested; i.e., the translated Fermi surfaces nearly overlap with the original ones. (b) The Fermi surfaces shown by the solid circles for large SOC ($\gamma \gg 1$), where the two Fermi surfaces have the same helicities (blue colors). The conventions are the same as above. (c) The overlap factor as a function of θ [denoting the position on the Fermi surface shown in (a)] in the transverse ($F^{-+}_{s;-s}$ with $s = \pm 1$) and longitudinal ($F^{LL}_{s;-s}$ with $s = \pm 1$) channels for small SOC in (a), where the length of the three arrow lines ending at the red dashed line, black dotted line, and the blue solid line correspond to the value of overlap factors as labeled nearby. The angles between the three arrows and Q correspond to the position on the Fermi surface shown by (a). (d) The overlap factor in the transverse ($F^{-+}_{-1;-1}$) and longitudinal ($F^{LL}_{-1;-1}$) channels for large SOC in (b). All the conventions are the same as in (c).

VII. NEARLY FERMI SURFACE NESTING CONDITIONS BETWEEN OUTER AND INNER FERMI SURFACE AT SMALL AND LARGE SOC

As we have shown above, the SSDW order turns into the LSDW order as the SOC strength $\gamma > 1.5$, which is a spin-flop transition. This change of the favorite SDW patterns for different SOC strengths can be understood by the different helicity of Fermi surfaces in two limiting cases with small and large SOC, where the helicity is defined as the eigenvalue of the SOC term $\vec{s}\cdot\vec{k}/|\vec{k}|$. In both cases, the two Fermi surfaces are nearly nested with the nesting wave vector $\vec{Q} = (k_{F2} - k_{F1})\hat{e}_z$ (actually the direction of wave vector $\vec{Q}$ is arbitrary). And this nesting condition is best satisfied near $\theta = 0,\pi$ where θ is the angle between the Fermi wave vector $\vec{k}_F$ and $\vec{Q}$ [schematically shown in Figs. 5(a) and 5(b)]. With SOC, the density and spin susceptibility are anisotropic due to the overlap factor $F_{sr}^{\mu\nu}$

defined in Eq. (14). For small SOC $\gamma \ll 1$, the two Fermi surfaces have different helicities (± 1). We find the overlap factor for the transverse susceptibility is $F^{-+}_{1;-1} = \cos^4(\theta/2)$, $F^{-+}_{-1;1} = \sin^4(\theta/2)$ which takes its maximum at $\theta = 0,\pi$, i.e., the place where the nesting condition is best satisfied; the overlap factor for the longitudinal susceptibility is $F^{LL}_{-1;1} = F^{LL}_{1;-1} = \sin^2\theta$ which is suppressed at $\theta = 0,\pi$ [see Fig. 5(c)]. As a result, the susceptibility is significantly enhanced in the transverse channel at the wave vector $|\vec{Q}| = k_{F2} - k_{F1}$, but suppressed in the longitudinal channel.

For large SOC $\gamma \gg 1$, the inner Fermi surface changes its helicity from 1 to -1, the overlap factor for transverse susceptibility is $F^{-+}_{-1;-1} = \frac{1}{4}\sin^2\theta$, and that for the longitudinal susceptibility is $F^{LL}_{-1;-1} = \cos^2\theta$ [see Fig. 5(d)]. In this case, the susceptibility is significantly enhanced in the longitudinal channel at the wave vector $|\vec{Q}| = k_{F2} - k_{F1}$ but suppressed in the transverse channel. This is consistent with the numerical calculations of the static susceptibility for different SOC strengths: the transverse susceptibility χ^{-+} reaches the maximum at $|\vec{Q}| = k_{F2} - k_{F1}$ for small SOC while the longitudinal susceptibility χ^{LL} reaches the maximum at $|\vec{Q}| = k_{F2} - k_{F1}$ for large SOC.

The nearly FS nesting conditions due to 3d SOC is a new feature of the SOC. It is the SOC which splits one FS into two with the Fermi momentum k_{F2} and k_{F1} [see Fig. 7(a)], which, in turn, leads to 4 possible FS nesting momenta $k_{F2} - k_{F1}, k_{F2} + k_{F1}, 2k_{F1}, 2k_{F2}$. Here, we find that in a 3d Weyl SOC system, the stripe SSDW and LSDW+CDW takes the FS nesting momentum $k_{F2} - k_{F1}$ as their ordering wave vector at a small or large SOC where the two Fermi surfaces have the same or opposite helicities, respectively (Fig. 5). In a sharp contrast, there could only be a $2k_F$ SDW due to FS nesting in some one- or quasi-one-dimensional metals without SOC [43]. There are no phenomena due to FS nestings in 2d or 3d itinerant systems without SOC. We expect that due to the FS nesting mechanism, the existences of the stripe SSDW and LSDW+CDW at small and large SOC strengths are robust and independent of the RPA approximations.

However, in the intermediate SOC strengths $0.5 < \gamma < 1.5$ in Fig. 2, the $\chi^{+-}(\vec{q},\omega = 0)$ is relatively flat in a finite-momentum regime due to the competitions from the multimomenta transfer processes, so it may lead to a coplanar SSDW with multimomenta ordering wave vectors. If so, the residual symmetry $[\mathrm{U}(1)^z_{\mathrm{spin}} \times \mathrm{U}(1)_{\mathrm{orbit}}]^{\alpha}_D \times (z \to z + \alpha/Q_T)$ left in the one-momentum SSDW at $\gamma < 0.5$ discussed in Sec. V is also broken. Then the symmetry-breaking pattern from the PM to this kind of multimomentum SSDW is $[\mathrm{SU}(2)_{\mathrm{spin}} \times \mathrm{SO}(3)_{\mathrm{orbit}}]_D \times \mathrm{Tran} \to 1$, so there are two Goldstone modes in this kind of SSDW state: one due to the symmetry breaking of $[\mathrm{U}(1)^z_{\mathrm{spin}} \times \mathrm{U}(1)_{\mathrm{orbit}}]$ and the other due to the translational symmetry breaking along the $\hat{z}$ axis.

VIII. FERMI SURFACE RECONSTRUCTIONS IN THE SSDW AND LSDW+CDW

From Eq. (12), if ignoring the Goldstone mode, one can see that the static SSDW $\langle\vec{\phi}_T\rangle = \phi_0(\cos Q_T z, \sin Q_T z, 0)$ provides a periodic potential with a reciprocal lattice vector $Q_T\hat{z}$ to the fermions. Figure 6(a) shows the evolution of the FS

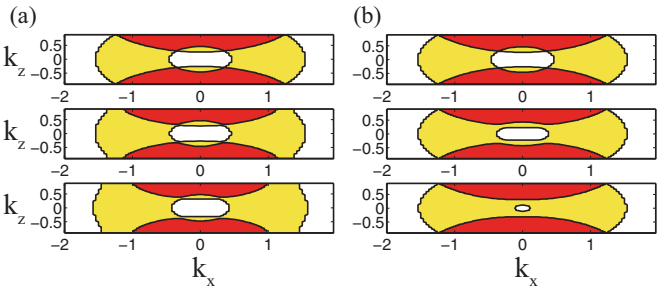

FIG. 6. The Fermi surface at $\gamma = 0.82$ and $Q = 1.8$ inside (a) the SSDW and (b) LSDW+CDW [44]. Due to the rotation symmetry about the k_z axis, we only show the $k_y = 0$ cross sections. From up to down, the order parameter is increasing as $\phi = 0,1,2$. The fermion occupation number in the red, yellow, white regime are 2, 1, 0 respectively. The intersections of FS at the BZ boundary split inside the SSDW, but not inside the LSDW+CDW. The intersections between large and small FS inside the BZ boundary split in both phases.

as the SSDW turns on near the PM-to-SSDW transition. There is a gap Δ^T_{BZ} opening at the BZ boundary. First-order degenerate perturbation shows that $\Delta^T_{BZ} = \phi_0 \cos^2\frac{\theta}{2}$ where θ is the polar angle of the crossing point between the FS and the first BZ boundary. There is also a gap Δ^T_I opening at the crossing between the outer FS and the inner FS inside the BZ. First-order degenerate perturbation shows that $\Delta^T_I = \phi_0|\cos\frac{\theta_1}{2}\cos\frac{\theta_2}{2}|$ where the $\theta_{1,2}$ are the two polar angles of the two crossing FS momenta $\vec{k}_{F1}, \vec{k}_{F2}$, respectively, satisfying $\vec{k}_{F2} - \vec{k}_{F1} = Q_T\hat{z}$.

Similarly, Fig. 6(b) shows the evolution of the FS as the LSDW turns on near the PM-to-LSDW transition. However, in sharp contrast to the SSDW, there is no gap opening at the BZ boundary $\Delta^L_{BZ} = 0$ which is also confirmed by the numerical calculations. There is still a gap Δ^T_I opening at the crossing between the outer FS and the inner FS inside the BZ. First-order degenerate perturbation shows that $\Delta^L_I = \frac{\phi_0}{2}|\sin\frac{\theta_1-\theta_2}{2}|$ where $\vec{k}_{F2} - \vec{k}_{F1} = Q_L\hat{z}$. The gap opening at $Q_c = 2Q_L$ due to the CDW can be similarly evaluated by degenerate perturbations and numerical calculations.

IX. SUMMARY AND DISCUSSION

In a recent work [18], we studied interacting fermions at a half filling in a 2d square lattice subject to Rashba SOC interaction ($\alpha = \beta$). In the strong-coupling limit, we find a collinear *Y*-*y* state [with ordering wave vector $(0,\pi)$] at a large SOC near $\alpha = \beta = \pi/2$, and a series of stripe commensurate coplanar spiral phases at a small SOC. The former may be the analog of the LSDW+CDW in the continuum limit at $\gamma > 1.5$. The latter may be the analog of the SSDW in the continuum limit at $\gamma < 0.5$. We also found there are multimomenta incommensurate coplanar spiral phases intervening between the commensurate coplanar spiral phases. As briefly discussed at the end of Sec. VII, they may be the analog of the multimomenta SSDW in the continuum limit at $0.5 < \gamma < 1.5$. In addition to the above collinear and coplanar phases in a 2d square lattice at the half filling, we also find some noncoplanar commensurate or incommensurate Skyrmion

crystals (IC-SkX) in the neighborhood of the collinear *Y-y* state. There are quantum commensurate-to-incommensurate (C-IC) Lifshitz transitions between the *Y-y* and the IC-SkX. However, these quantum Lifshitz transitions are driven by the touchdowns of the C-IC magnons at isolated ordering wave vectors, in contrast to the continuous manifold in Eqs. (18) and (20). In the weak-coupling limit, one gets a mixed phase of a spin-orbital-correlated magnetic ordering coexisting with gapless Dirac fermions. So there must be some quantum phase transitions from the weak to the strong coupling limit. Here, in the continuum limit, due to the FS nesting conditions at small and large SOC, we established that it is the coplanar SSDW at small SOC $\gamma < 0.5$ and the collinear LSDW+CDW at large SOC $\gamma > 1.5$. There could be some multimomenta coplanar SSDW sandwiched between the two phases.

Note that the quantum critical theory from the normal to FM (or AFM) transition even without SOC is still not completely understood. There are alternative scenarios in itinerant Fermi systems without SOC [45–47]. A more refined Ginzburg-Landau theory than Hertz-Millis theory should treat both the order parameter fluctuations and the gapless fermions [48,49] on the same footing and remains to be constructed. However, we expect that the dramatic SOC effects discovered in this work, especially due to the FS nesting effects at small or large SOC, dominate over all the subtle effects discussed in [45,46], so the quantum Lifshitz theory and associated Fermi-surface reconstructions remain robust against all these subtle effects. This is to say, the dominant roles played by the SOC may make the magnetic transitions in itinerant Fermi systems with the SOC simpler than its counterpart without it.

We achieved the global phase diagram Fig. 2 by exact symmetry statements, followed by the RPA calculations. However, we neglect possible competition from nonmagnetic states or even possible fractionalized Fermi liquid FL* or SDW* states [45,46]. In Fermi systems without SOC, nonmagnetic states with strong local correlations have been constructed to suppress the exchange energy [50]. These nonmagnetic states may compete with the FM, SSDW, or LSDW+CDW state. In the presence of SOC, it remains interesting to construct suitable nonmagnetic states incorporating the short-range correlations to compete with all the states studied in this paper. We expect the new mechanism, some exact statements, and appealing physical picture discussed here to realize the itinerant SSDW or LSDW+CDW maybe robust against these possible nonmagnetic states. We expect the dramatic SOC effects to dominate over possible nonmagnetic states, especially at the small and large SOC strengths leading to the LSDW+CDW phase. However, the SSDW with multiple-momenta orderings in the intermediate SOC $0.5 < \gamma < 1.5$ may be more vulnerable to these nonmagnetic or even fractionalized FL* or SDW* states. Different methods or approaches are needed to confirm or dispute the expectations. Unfortunately, the SOC makes the sign problem in the QMC much more serious than that without SOC.

In view of very recent experimental realizations of the 2d Rashba SOC [7–10], the 3d Weyl SOC can be straightforwardly realized in near-future experiments. In a ^{6}Li system, the two hyperfine sublevels $|1/2,-1/2\rangle$ and $|1/2,1/2\rangle$ can be chosen as two pseudo-spin-1/2 states. With $N \sim 10^4$ ^{6}Li atoms inside an isotropic trap with a trap frequency $2\pi \times 10$ Hz, and a typical magnetic field gradient strength $\nabla B = 0.09\ \mathrm{G}/\mu\mathrm{m}$ (within practical range [51]), we estimate $\gamma \sim 1.82$. It falls into the LSDW regime [Fig. 2(b)] with the orbital momentum $Q_L \sim 0.13 k_R$. The critical interaction strength $k_F a_c \sim 0.12$ is an order of magnitude smaller than the value π [Fig. 2(a) at $\gamma = 0$] for a possible FM at the same density without the SOC [20,25].

Finally, it is simple to incorporate the effects of a harmonic trap. Taking the local density approximation, the chemical potential (or equivalently the local density) will decrease from the trap center to zero to the boundary, so the $\gamma = k_R/k_F$ will also decreases from the center to the edge. Assuming $\gamma = 1.82$ at the center, then one will observe the shell structures of LSDW+CDW near the trap center surrounded by SSDW near the edge. So experiments could reach SSDW or LSDW+CDW at weak interactions which can make heating issues [7–10] under even better control. This fact may be important for the experimental observation of the phenomena discussed here in the future.

In short, the SOC leads to dramatic changes in essentially all the physical quantities such as the quantum phases, excitation spectra, and universality classes of quantum and classical phase transitions. All the novel phenomena can be probed by various established experimental techniques [5,26–31]. For example, the collective excitations in the PM [Fig. 1(b)], SSDW, and LSDW+CDW can be detected by the angle-resolved Bragg spectroscopy [30,31], the order parameters $\vec{\phi}_{T/L}$ in Fig. 3 may be directly measured by time-of-flight experiments, and the evolution of the FS topology in Fig. 6 can be monitored by spin-injection radio frequency spectroscopy [5].

ACKNOWLEDGMENTS

J.Y. thanks Fadi Sun and Yi-Xiang Yu for helpful discussions, especially the former for collaboration in studying interacting spinor bosons or fermions with SOC on lattices. J.Y.'s research was supported by NSF-DMR-1161497, and at KITP is supported by NSF PHY11-25915. This work was also supported by the NKBRSFC under Grants No. 2011CB921502 and No. 2012CB821305, NSFC under Grants No. 61227902, No. 61378017, and No. 11434015, and SPRPCAS under Grant No. XDB01020300.

APPENDICES

In Appendix A, we contrast the collective modes in the paramagnet with the SOC which breaks inversion symmetry and those in the conventional FM state without SOC which break time-reversal symmetry. In Appendix B, we contrast the Hertz-Millis type of action to describe magnetic transitions in itinerant Fermi systems without SOC with that in the itinerant Fermi systems with SOC to describe the magnetic transition from the paramagnet to a putative FM. We identify the mechanism to lead to the quantum Lifshitz action to describe the transition from the paramagnet to the SSDW discussed in the main text. In Appendix C, we contrast the Fermi surface reconstruction inside the SSDW with that in the LSDW+CDW.

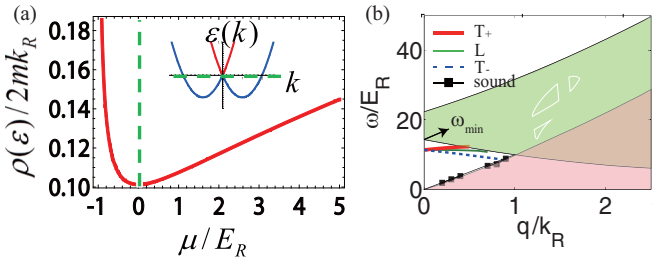

FIG. 7. (a) The density of states $\rho(\epsilon)$ (per volume) in units of $2mk_R$ at the chemical potential μ. The green dashed line denotes $\mu = 0$ (equivalent to $\gamma = 0.63$) as shown by the inset. (b) Collective modes for 3d Fermi gas with Weyl-type SOC in the normal side. The parameters here are $\mu/E_R = 20$ (equivalent to $\gamma = 0.21$) which corresponds to case iii in Fig. 8 and $a_s = 0.9a_s^c$. The green (yellow) region is the intraband (interband) particle-hole excitation continuum. $\omega_{\min}$ denotes the lower edge of the interband particle-hole continuum, which is taken as the unit in Fig. 8(d). In fact, (b) is a redrawing of Fig. 1(b) in the helicity basis. Namely, folding Fig. 1(b) left $q_z < 0$ back to the right $q_z > 0$ and changing the q_z axis to the q axis leads to (b). Alternatively, picking $\vec{q}$ along the $\hat{z}$ axis and inverting with respect to the origin gives back Fig. 1(b).

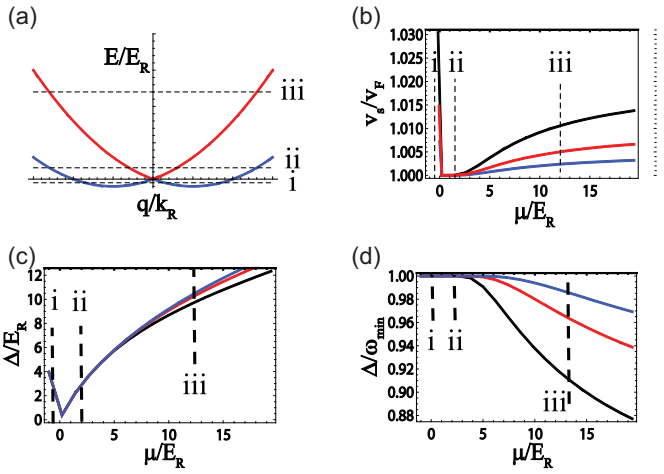

FIG. 8. (a) Two split Fermi surfaces due to the Weyl SOC at the noninteracting limit. Shown are different filling cases by the dashed lines i, ii, and iii. (b) The ratio v_s/v_F of gapless sound mode. (c) The Δ/E_R and (d) $\Delta/\omega_{\min}$ show the energy gap at $q = 0$ for the three gapped modes. The three different colors represent different interaction strengths, i.e., black (critical interaction strength g_c for the putative FM phase transition), red ($g = 4/5g_c$), and blue ($g = 2/3g_c$).

APPENDIX A: COLLECTIVE MODES AND P-H EXCITATIONS FOR 3D FERMI GAS WITH AND WITHOUT SOC AT THE RPA LEVEL

In this Appendix, we apply the RPA formalism to calculate the collective modes in the paramagnet side with the Weyl SOC and also those in the FM side of Fermi gas without SOC. It is instructive to compare the two cases: the former has explicit inversion-symmetry breaking, the latter the spontaneous time-reversal-symmetry breaking. It is also shown in the main text that the FM state is always superseded by SSDW or LSDW+CDW, so never a ground state in the former system, but it maybe a ground state in the latter.

1. Collective modes in the paramagnet side with SOC: Inversion-symmetry breaking

As shown in Sec. II, the $[\mathrm{SU}(2)_{\mathrm{spin}} \times \mathrm{SO}(3)_{\mathrm{orbit}}]_D$ symmetry [12,16] dictates that the dynamical 4×4 density-spin susceptibility Eq. (14) can be split into two 2×2 subspaces: (i) n-L subspace formed by the density and the longitudinal spin mode, and (ii) T_1-T_2 subspace formed by the two transverse modes. This exact decomposition simplifies the following analytical and numerical calculations considerably.

The gapless sound mode in the n-L subspace, $\omega_s = v_s q$ in Fig. 7(b), is determined by the pole of 2×2 density-spin susceptibility: $\det(1 + \frac{g}{4}\sigma_z \chi_{nL}) = 0$ with

$$\chi_0^{nL}(\vec{q},\omega) = \frac{m\left(k_1^2 + k_2^2\right)}{2\pi^2\kappa} \times \begin{pmatrix} F(y) & \beta y F(y) \\ \beta y F(y) & \frac{1}{3} + \frac{\sqrt{k_R^2+2m\mu}}{3k_R}\beta + y^2 F(y) \end{pmatrix}, \tag{A1}$$

where $k_2 > k_1$ are the two Fermi momenta in Fig. 8(a), $2\kappa = k_1 + k_2$ $(k_2 - k_1)$ for $\mu > 0$ $(\mu < 0)$, $\beta = \frac{k_2^2 - k_1^2}{k_2^2 + k_1^2}$ and $y = \omega/v_F q$, v_F the Fermi velocity, $F(y) = 1 - y\,\mathrm{arccoth}\, y$. It is easy to see that Eq. (A1) indeed satisfies the constraints Eq. (10) and (11). We numerically determined the velocity v_s of this gapless sound mode at $\mu/E_R = 20$ shown in Fig. 8(b). This sound mode corresponds to a coupled density-longitudinal spin fluctuation.

At the RPA level, from Eq. (3), the two transverse modes are determined by

$$1 - \frac{g}{2}\chi_0^{+-}(\vec{q},\omega) = 0, \quad 1 - \frac{g}{2}\chi_0^{-+}(\vec{q},\omega) = 0, \tag{A2}$$

where $\chi_0^{+-}(\vec{q},\omega) = 2(\chi^{xx} - i\chi^{xy})$ is given by Eq. (14). Equation (A2) lead to the $T_\pm$ mode in Fig. 7(b).

In all, there are three branches of the gapped mode, one L mode within the n-L subspace and the other two $T_\pm$ modes within the T_1-T_2 subspace. Due to the $\mathrm{SU}(2)_{\mathrm{spin}}$ symmetry at $\vec{q} = 0$, the three gapped modes are degenerate at $\vec{q} = 0$ where the gap Δ is determined by $\det[1 - \frac{g}{4}\chi_{\mathrm{spin}}(\omega,\vec{q} = 0)] = 0$, with

$$\chi_{\mathrm{spin}}^{ij}(\omega,\vec{q} = 0) = \frac{m}{6\pi^2 k_R} \times \left(k_2^2 - k_1^2 + \frac{m^2\omega^2}{4k_R^2}\ln\left[\frac{4k_R^2k_2^2 - m^2\omega^2}{4k_R^2k_1^2 - m^2\omega^2}\right]\right) \times \delta^{ij}, i,j = x,y,z. \tag{A3}$$

The numerical result of this energy gap Δ at different μ/E_R is shown in Fig. 8(c) (in units of the recoil energy $E_R = k_R^2/2m$) and Fig. 8(d) [in units of the lower edge of interband particle-hole excitation energy $\omega_{\min}$ shown in Fig. 7(b)].

In Fig. 8(a), we plot three typical filling cases shown by the dashed lines: (i) the dilute-density case with $\mu < 0$; (ii) $\mu > 0$ but close to the Dirac point ($\mu = 0$); (iii) the dense-density case. Figure 7(b) belongs to case iii. In Fig. 8(b), as the filling tends to the Dirac point from above $\mu > 0$, the

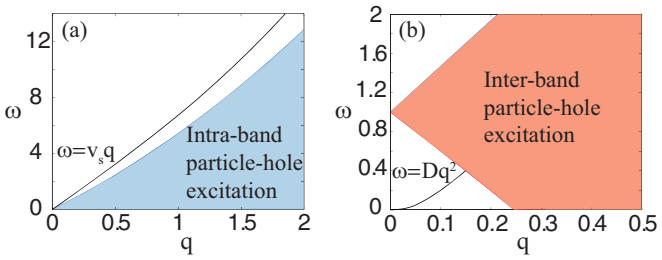

FIG. 9. The particle-hole continuum and collective modes in traditional Fermi gas without SOC. (a) Zero sound in the normal side and (b) only the T_+ mode is shown in the FM side.

v_s/v_F decreases close to 1. After passing the Dirac point, the ratio increases. In Fig. 8(c), the Δ/E_R decreases close to zero around the Dirac point [note that at the Dirac point, the blank regime between the interband and intraband particle-hole excitation shown in Fig. 7(b), which is the regime free of PH excitations, shrinks to zero]. After passing the Dirac point, the ratio increases also. To show the relationship between the energy gap Δ and the P-H excitation, in Fig. 8(d) we show $\Delta/\omega_{\min}$ with $\omega_{\min}$ the lower edge of the interband particle-hole excitation energy shown in Fig. 7(b). We find as the chemical potential decreases from iii to i, the ratio approaches 1 from below, namely, the gapped collective modes move more closer to the edge of interband particle-hole excitation continuum in Fig. 7(b). Indeed, in the strong-SOC limit $\mu \to -1$, the sound velocity saturates $v_s/v_F \simeq 1.102$, the energy gap Δ increases and moves close to the P-H continuum $\Delta/E_R \simeq 4(1-\sqrt{1+\mu})$.

2. Collective modes in the FM without SOC: Time-reversal-symmetry breaking

As analyzed in Sec. III, in the normal phase of SOC, it is the I-symmetry breaking in the SOC Hamiltonian which leads to the $T_\pm$ split shown in Fig. 7(b). However, in the FM of conventional system, it is the spontaneous T-symmetry breaking which leads to the split $T_\pm$ in Fig. 3(b) where only T_+ is shown. So the two splitting mechanisms are complementary to each other. Here it is instructive to perform a detailed calculation on the $T_\pm$ mode in the FM of conventional system. Very surprisingly, to the best of the authors' knowledge, there is no previous literature to discuss this important and tricky physical picture.

On the normal side, due to the $\mathrm{SU}(2)_{\mathrm{spin}} \times \mathrm{SO}(3)_{\mathrm{orbit}}$ symmetry, the density and spin are decoupled; the density and spin susceptibility are $\chi^{\mu\nu} = \chi_0 \delta^{\mu\nu}$ where $\mu,\nu = n,s_x,s_y,s_z$. Since the interaction is repulsive (attractive) in the density (spin) channel, there is only one gapless density mode with linear dispersion $\omega_q = v_s q$, i.e., zero sound in the density channel, no stable collective modes in the spin channel [Fig. 9(a)].

On the FM side, there is a spin polarization $\vec{M}$ along $\hat{z}$; the symmetry-breaking pattern is $\mathrm{SU}(2)_{\mathrm{spin}} \to \mathrm{U}(1)_z$ which leads to Eq. (3) for any $\vec{q}$. One still has inversion symmetry I which leads to Eq. (15). The fermion propagator takes the form

$$\mathcal{G}(i\omega_n,\vec{k}) = \frac{1}{2}\sum_{s=\pm 1} \frac{\sigma_0 + s\sigma_z}{i\omega_n - \vec{k}^2/2m + sgM/4}. \quad \text{(A4)}$$

As said above, the remaining symmetry $\mathrm{U}(1)_z$ dictates that the density-spin susceptibility $\chi^{\mu\nu},\mu,\nu = n,s_x,s_y,s_z$, can be decoupled to two 2×2 matrices: one for the density and longitudinal spin mode $\hat{L} = \vec{M}/M$, another for the two transverse spin modes $\hat{T}_1 \cdot \vec{M} = \hat{T}_2 \cdot \vec{M} = 0$. In the density-longitudinal subspace, the density fluctuation is strongly coupled with the longitudinal spin fluctuation, and the 2×2 susceptibility takes the form

$$\chi^{nL} = \chi_0 \begin{pmatrix} 1 & -1 \\ -1 & 1 \end{pmatrix}, \quad \text{(A5)}$$

where $\chi_0 = \frac{mk_F^2}{4\pi^2}(2 + y \ln\frac{y-1}{y+1})$ with $y = m\omega/k_F q$. Due to the absence of any poles in $\det[1 + \frac{g}{4}\sigma_z \chi^{nL}] = 0$, there are no collective modes in the n-L subspace.

However, in the transverse (T_1,T_2) subspace, Eq. (3) still holds, and there is only one low-energy collective mode: the T_+ mode $\omega_q = Dq^2$ at small $\vec{q}$ from the pole of χ^{+-}, which couples only to the interband P-H excitations at higher q [Fig. 9(b)], while the T_- mode from the pole of χ^{-+} has higher energy and also higher threshold momentum, and can be dropped [not shown in Fig. 9(b)].

In short, in the paramagnetic phase with the SOC, it is the explicit I-symmetry breaking of the SOC Hamiltonian which leads to the $T_\pm$ split shown in Fig. 7(b). However, in the FM of the conventional system, it is the spontaneous T-symmetry breaking which leads to the $T_\pm$ split in Fig. 3(b). So the two splitting mechanisms are complementary to each other.

APPENDIX B: CONTRAST OF HERTZ-MILLIS THEORY WITHOUT SOC WITH THE QUANTUM LIFSHITZ TRANSITIONS WITH SOC

In this section, we first review the Hertz-Millis theory with the symmetry group $\mathrm{SU}(2)_{\mathrm{spin}} \times \mathrm{O}(3)_{\mathrm{orbit}}$ to describe the magnetic transitions in itinerant electron systems without SOC. Then we construct the quantum bosonic Lifshitz theory with SOC and the reduced symmetry group $[\mathrm{SU}(2)_{\mathrm{spin}} \times \mathrm{O}(3)_{\mathrm{orbit}}]_D$ to describe the paramagnet to the putative FM transition which is dramatically different from the Hertz-Millis theory.

1. Hertz-Millis theory to describe magnetic phase transition without SOC

The possible ferromagnetism (FM) in an itinerant fermion system with a repulsive interaction is a long-standing problem in condensed matter physics dating back to Stoner's FM instability. Hertz [20] constructed a quantum Ginzburg-Landau theory to study magnetic fluctuations near the itinerant paramagnet to itinerant FM transition. The quadratic term in Hertz's action reproduces Stoner's FM instability. Millis [21] performed RG calculations on the Hertz theory at finite T and mapped out rich quantum-classical crossover regimes on the T-δ phase diagram where δ is the tuning parameter of the transition.

In Fermi systems without SOC, the density and spin channels are decoupled. There are collective excitations in the density channel only, but none in the spin channel. So in discussing possible magnetic orders, one only need focus on the possible instability in the P-H channel; this is what Hertz and Millis did in [20,21]. So when looking at the long-

wavelength, long-energy limit, Hertz and Millis studied the $\vec{q} \to 0$ limit, then $\omega/qv_F \to 0$. This limit is justified, because it captures the dominant spin-spin correlation spectral weights near the magnetic transition. In this $\vec{q} \to 0, \omega/qv_F \to 0$, Hertz derived the following action in terms of the spin fluctuation order parameter $\vec{\phi}$:

$$\mathcal{S}[\vec{\phi}] = \frac{1}{2\beta}\sum_n \int \frac{d\vec{k}}{(2\pi)^2}(\delta + \gamma y + \alpha q^2)\vec{\phi}^2 + u\int d\vec{r}d\tau(\vec{\phi}^2)^2, \tag{B1}$$

where $y = |\omega_n|/v_F q$ for FM and $y = c|\omega_n|$ for the (π,π) AFM where all the momenta are measured relative to (π,π); the $\delta = 1/g - \chi_{\rm spin}(\vec{q} \to 0, \omega/qv_F \to 0)$ is the controlling parameter tuning the paramagnet to the ferromagnet transition. When $\delta_s > 0$, it is in the paramagnet side; when $\delta_s < 0$, it is in the ferromagnetic side.

Under the scaling transformation $q \to q'/b, T \to T'/b^z$ where the dynamic exponent $z = 3$ for the FM and $z = 2$ for the AFM, it is easy to see that at the tree level, $\delta' = \delta b^2, \gamma_T' = \gamma_T, u' = ub^{4-d-z}$. Because $4 - (d + z) < 0$ in 3d, so $d = 3$ is above the upper critical dimension, the u is always (dangerously) irrelevant, which may lead to violations of scalings near a quantum critical point [52]. However, it is the dangerously irrelevant coupling u which leads to interesting quantum-classical crossover regimes on the T-δ phase diagram.

2. The effective action to describe the PM to the putative FM transition Eq. (17)

However, as stated in the main text, the above Hertz-Millis theory completely breaks down in the presence of SOC. Indeed, in the effective Hertz-Millis action Eq. (B1), all three spin components are the same due to the $\mathrm{SU(2)_{spin}} \times \mathrm{O(3)_{orbit}}$ symmetry in the paramagnet side. However, as shown in the main text, the symmetry with the Weyl SOC is reduced to $[\mathrm{SU(2)_{spin}} \times \mathrm{O(3)_{orbit}}]_D$, so one has to distinguish not only the longitudinal mode, but also the two split transverse modes T_+ and T_-.

As stated in the main text, in constructing a quantum Ginzburg-Landau action to describe the paramagnet to the putative FM transition, one needs to take the $\mathbf{q} \to 0, \omega/v_F q \to 0$ limit to capture the dominant critical spin-fluctuation spectral weights. Taking this limit in the n-L space in Eq. (A1) leads to

$$\chi_0^{nL}(\vec{q}, i\omega_n) = \frac{m(k_1^2 + k_2^2)}{2\pi^2\kappa}\begin{pmatrix} 1 - \frac{\pi}{2}|y_n| - \alpha_n q^2 & -i\beta y_n \\ -i\beta y_n & \frac{1}{3} + \frac{\sqrt{k_R^2 + 2m\mu}}{3k_R}\beta - y_n^2 - \alpha_L q^2 \end{pmatrix}, \tag{B2}$$

where all the parameters are listed below Eq. (A1). Because the density fluctuation is noncritical across the phase transition point, integrating it out leads to

$$\mathcal{S}_L^{(2)} = \frac{1}{2}\int \frac{d^3\vec{q}}{(2\pi)^3} T\sum_n (\delta + \gamma_L y_n^2 + \alpha_L q^2)|\phi_L(\vec{q}, i\omega_n)|^2, \tag{B3}$$

where $\delta = \frac{1}{g} - \frac{\chi_0}{4}$ is the tuning parameter of the transition, and $\gamma_L = \frac{m(k_1^2+k_2^2)}{8\pi^2\kappa}(1 - \eta)$ with $\eta = \frac{gm(k_1^2+k_2^2)}{8\pi^2\kappa + gm(k_1^2+k_2^2)}\beta^2 < 1$ as the modification from the density fluctuations. One can extract the longitudinal propagator $\mathcal{G}_L^{-1} = \delta + \gamma_L y_n^2 + \alpha_L q^2$.

In the $\mathbf{q} \to 0, \omega/v_F q \to 0$ limit, the action in the transverse spin subspace is reduced to

$$\mathcal{S}_T^{(2)} = \frac{1}{2}\int \frac{d^3\vec{q}}{(2\pi)^3} T\sum_n (\phi_+^*, \phi_-^*)\begin{pmatrix} \delta + \gamma_T^0|y_n| + \beta_T q + \alpha_T q^2 & 0 \\ 0 & \delta + \gamma_T^0|y_n| - \beta_T q + \alpha_T q^2 \end{pmatrix}\begin{pmatrix}\phi_+ \\ \phi_-\end{pmatrix}, \tag{B4}$$

where $\gamma_T^0 = \frac{m(k_1^2+k_2^2)}{32\pi\kappa}$ and one can extract the transverse propagators $\mathcal{G}_{T_\pm}^{-1} = \delta + \gamma_T^0|y| \pm \beta_T q + \alpha_T q^2$.

Note that the $\mathrm{SU(2)_{spin}}$ symmetry at $\vec{q} = 0$ dictates that there is only one tuning parameter δ from the PM to the putative FM transition in the actions Eqs. (B3) and (B4). When $\delta > 0$, it is in the PM phase. When $\delta < 0$, it is in the putative FM phase. Equations (B3) and (B4) reached at the RPA level satisfy the exact relations Eqs. (3), (4) and Eqs. (7), (8), respectively. The combination of Eq. (B3) and Eq. (B4) leads to the quadratic part of the effective action Eq. (17) in the main text. As argued in the main text, it is the $-\beta_T q$ term in the ϕ_- propagator which leads to the instability of the putative FM state and the quantum Lifshitz-type transition from the PM to the SSDW.

The most relevant interaction is the fourth-order term with the general form $U_{ijkl}\phi^i\phi^j\phi^k\phi^l$. We expect that the leading relevant coupling among all the possible fourth-order terms should be momentum and frequency independent $(\vec{\phi}^2)^2$ which has a larger symmetry $\mathrm{SU(2)_{spin}} \times \mathrm{O(3)_{orbit}}$ than the kinetic terms. We checked this expectation through direct calculations of the coefficient U_{ijkl}, which are found to be given by linear combinations of factors such as $\delta_{ij}\delta_{kl}$, $\delta_{ik}\delta_{jl}$, and $\delta_{il}\delta_{kj}$. All of these factors lead to the $\mathrm{SU(2)_{spin}} \times \mathrm{O(3)_{orbit}}$ invariant fourth-order term $u\int d^3\vec{r}[\vec{\phi}^2(\vec{r})]^2$ in Eq. (17).

APPENDIX C: FERMI SURFACE RECONSTRUCTIONS IN THE PRESENCE OF SDW ORDER

In this Appendix, we first analyze the symmetries of the SSDW and the LSDW+CDW states and their implications for the degeneracy at both the BZ boundary and the Dirac point

$k = 0$ in Fig. 8(a). Then we will evaluate the gap openings at the BZ boundary by degenerate perturbation theory.

1. Symmetry analysis at the BZ boundaries and the Dirac point

We first summarize the remaining symmetries of two types of SDW orders. Both the SSDW and LSDW order are invariant under a combined transformation of (1) $[\mathrm{U}(1)^z_{\mathrm{spin}} \times \mathrm{U}(1)_{\mathrm{orbit}}]_D$; (2) $\mathcal{P}_x, \mathcal{P}_y, \mathcal{P}_z$; (3) the time-reversal symmetry with a translation $\mathrm{Tr}(a)$ where a is a suitably chosen distance along the $\hat{z}$.

For the SSDW $\vec{\phi}_T = \phi_0(\cos Qz, \sin Qz, 0)$, the $[\mathrm{U}(1)^z_{\mathrm{spin}} \times \mathrm{U}(1)_{\mathrm{orbit}}]^{\alpha}_D \times (z \to z + \alpha/Q_T)$ symmetry dictates that the spectrum is rotational symmetric about the k_z axis. So we can set $k_y = 0$. The SSDW order preserves the $\mathcal{P}_x$ and the $\mathcal{P}'_y = \mathcal{P}_y + T_r(\frac{\pi}{Q})$ symmetry where the prime in the subscript indicates an combined translation. Under $\mathcal{P}_x$ ($\mathcal{P}'_y$), the single-particle eigenstates with a given momentum $\vec{k}$ belonging to the first Brillouin zone (BZ) are mapped to the same $\vec{k}$ only when $k_z = -Q/2$ (BZ boundary) or $k_z = 0$. Any eigenwave function at the BZ boundary can be written as

$$|\Psi\rangle_{BZ} = \sum_{n,\sigma} a_{n\sigma} |(n + 1/2)Q, \sigma\rangle, \tag{C1}$$

where $(n + 1/2)Q$ represents the k_z component of $\vec{k}$, $\sigma = 1,2$ the index of spin component. Here and after, we drop the $k_x, k_y = 0$ component in $|\vec{k}, \sigma\rangle$ unless it is specialized. By the same convention, the wave function at $k_z = 0$ can be written as

$$|\Psi\rangle_0 = \sum_{n,\sigma} b_{n\sigma} |nQ, \sigma\rangle. \tag{C2}$$

Since the Hamiltonian is real, the coefficients $a_{n\sigma}$ and $b_{n\sigma}$ can be chosen to be real values. Applying $\mathcal{P}_x$ to $|\Psi\rangle_{BZ}$ and $|\Psi\rangle_0$ twice leads to $\mathcal{P}_x^2 |\Psi\rangle_{BZ} = |\Psi\rangle_{BZ}$ and $\mathcal{P}_x^2 |\Psi\rangle_0 = |\Psi\rangle_0$. This property is not sufficient to guarantee the twofold degeneracy at both the BZ boundary and $\vec{k} = 0$. When applying $\mathcal{P}'_y$, we also set $k_x = 0$ (namely at the center of the BZ boundary and $\vec{k} = \vec{0}$) and find $\mathcal{P}'^2_y |\Psi\rangle_{BZ} = |\Psi\rangle_{BZ}$ and $\mathcal{P}'^2_y |\Psi\rangle_0 = -|\Psi\rangle_0$. The later relation ensure the twofold degeneracy of the energy spectrum at $\vec{k} = 0$. So the Dirac cone at $\vec{k} = 0$ remains inside the SSDW.

The LSDW with $\vec{\phi}_L = \phi_0(0, 0, \cos Qz)$ preserves the $\mathcal{P}'_x = \mathcal{P}_x + T_r(\frac{\pi}{Q})$ and $\mathcal{P}'_y = \mathcal{P}_y + T_r(\frac{\pi}{Q})$ symmetry. Any eigenwave functions at the BZ boundary and $\vec{k} = 0$ are also given by Eqs. (C1) and (C2), respectively. Since the Hamiltonian is real, all of coefficients $a_{n\sigma}$ and $b_{n\sigma}$ can be chosen to be real. Applying the $\mathcal{P}'_x$ symmetry leads to $\mathcal{P}'^2_x |\Psi\rangle_{BZ} = -|\Psi\rangle_{BZ}$ and $\mathcal{P}'^2_x |\Psi\rangle_0 = |\Psi\rangle_0$. The former relation ensures the twofold degeneracy of the energy spectrum at the BZ boundary. Similarly to the case for the SSDW discussed above, applying the $\mathcal{P}'_y$ symmetry ensures the twofold degeneracy at $\vec{k} = 0$. So the Dirac cone at $\vec{k} = 0$ remains inside the LSDW.

As we have shown in the main text, the LSDW order would induce a CDW order with the orbital momentum $2Q_L$. Because the density order is invariant under the above symmetry operations, all of these results would not change.

2. Gap opening at the BZ boundary and inside the BZ by the degenerate perturbation theory

(1) *At the BZ boundaries*. At the BZ boundary, the $|(n + \frac{1}{2})Q, s\rangle$ and $|-(n + \frac{1}{2})Q, s\rangle$ with the same helicity s form a degenerate pair. For the SSDW, the 2×2 matrix in the two lowest bands with $n = 0, s = -1$ is given by

$$\mathcal{H}_{SSDW} = \begin{pmatrix} \mu & -\frac{\phi_0}{2} \sin^2 \frac{\theta}{2} e^{-i\varphi} \\ -\frac{\phi_0}{2} \sin^2 \frac{\theta}{2} e^{i\varphi} & \mu \end{pmatrix}, \tag{C3}$$

where $\mu = \xi_{Q/2,-}$, θ, φ is the azimuthal angle of $k = (k_x, 0, Q/2)$ with $\theta < \pi/2$. The spectrum is given by

$$\xi_s = \xi_{Q/2,-} + s \frac{\phi_0}{2} \sin^2 \frac{\theta}{2}, \tag{C4}$$

with the band gap $\Delta = \phi_0 \sin^2 \frac{\theta}{2}, \theta < \pi/2$.

Similarly for $k = (k_x, 0, -Q/2)$ with $\theta > \pi/2$, we obtain the band gap $\Delta = \phi_0 \cos^2 \frac{\theta}{2}, \theta > \pi/2$. By contrast, for the LSDW order, there is no matrix element between $|(n + \frac{1}{2})Q, s\rangle$, and $|-(n + \frac{1}{2})Q, s\rangle$ is always zero. So there is no band gap opening to this order. In fact, the above exact symmetry dictates there is no gap opening to any order of perturbations.

(2) *At the intersections between the large and small FS inside the BZ*. The SOC leads to the splitting of the FS into two with opposite helicities. When there is an intersection between them inside the BZ, the states $|k + nQ, r\rangle$ and $|k + mQ, s\rangle$ are coupled together. If $m - n = \pm 1$, the 2×2 matrix in the two degenerate levels is

$$\mathcal{H}_{T/L-SDW} = \begin{pmatrix} \mu & \phi_0 M \\ \phi_0 M^* & \mu \end{pmatrix}, \tag{C5}$$

where μ is the Fermi energy, $M = \frac{1}{2}\langle k_1, s|\sigma^+|k_2, r\rangle$ for the SSDW, while $M = \frac{1}{4}\langle k_1, s|\sigma^z|k_2, r\rangle$ for the LSDW. The band gap is given by $\Delta = 2\phi_0|M|$.

At small γ, the two intersecting FS have opposite helicities $s = -r = 1$. For the SSDW order, $M = -\frac{1}{2} \cos \frac{\theta_1}{2} \cos \frac{\theta_2}{2} e^{i\varphi_2}$, where $\theta_{1,2}, \varphi_1 = \varphi_2$ are the polar and azimuth angles of $k_{1,2}$, while for LSDW, $M = \frac{1}{4}(\cos \frac{\theta_1}{2} \sin \frac{\theta_2}{2} - \sin \frac{\theta_1}{2} \cos \frac{\theta_2}{2}) = -\frac{1}{4} \sin \frac{\theta_1 - \theta_2}{2}$.

At large γ, the two intersecting FS have the same helicities $s = r = -1$. For the SSDW, $M = -\frac{1}{2} \sin \frac{\theta_1}{2} \cos \frac{\theta_2}{2} e^{i\varphi_2}$, while for the LSDW, $M = \frac{1}{4}(\sin \frac{\theta_1}{2} \sin \frac{\theta_2}{2} - \cos \frac{\theta_1}{2} \cos \frac{\theta_2}{2}) = -\frac{1}{4} \cos \frac{\theta_1 + \theta_2}{2}$.

[1] J. Ye, Y. B. Kim, A. J. Millis, B. I. Shraiman, P. Majumdar, and Z. Tešanović, Phys. Rev. Lett. **83**, 3737 (1999).

[2] M. Z. Hasan and C. L. Kane, Rev. Mod. Phys. **82**, 3045 (2010).

[3] X. L. Qi and S. C. Zhang, Rev. Mod. Phys. **83**, 1057 (2011).

[4] A. M. Turner and A. Vishwanath, arXiv:1301.0330.

[5] Y. J. Lin, K. Jiménez-García, and I. B. Spielman, Nature (London) **471**, 83 (2011); P. Wang, Z. Q. Yu, Z. Fu, J. Miao, L. Huang, S. Chai, H. Zhai, and J. Zhang, Phys. Rev. Lett. **109**, 095301 (2012); L. W. Cheuk, A. T. Sommer, Z. Hadzibabic, T. Yefsah, W. S. Bakr, and M. W. Zwierlein, *ibid.* **109**, 095302 (2012); For a review, see J. Dalibard, F. Gerbier, G. Juzeliūnas, and P. Öhberg, Rev. Mod. Phys. **83**, 1523 (2011).

[6] There is a recent experimental investigation of magnetic phases of spin-1 ^{87}Rb spinor BEC subject to a 1d SOC in the presence of both vector and tensor Zeeman couplings; D. L. Campbell, R. M. Price, A. Putra, A. Valdés-Curiel, D. Trypogeorgos, and I. B. Spielman, Nat. Commun. **7**, 10897 (2016).

[7] Lianghui Huang *et al.*, Nat. Phys. **12**, 540 (2016).

[8] Zengming Meng *et al.*, arXiv:1511.08492.

[9] M. L. Wall, A. P. Koller, S. Li, X. Zhang, N. R. Cooper, J. Ye, and A. M. Rey, Phys. Rev. Lett. **116**, 035301 (2016).

[10] Zhan Wu *et al.*, arXiv:1511.08170.

[11] J. P. Vyasanakere and V. B. Shenoy, Phys. Rev. B **83**, 094515 (2011); J. P. Vyasanakere, S. Zhang, and V. B. Shenoy, *ibid.* **84**, 014512 (2011).

[12] Yu Yi-Xiang, Jinwu Ye, and W. M. Liu, Phys. Rev. A **90**, 053603 (2014).

[13] Y. Li and C. Wu, Phys. Rev. B **85**, 205126 (2012).

[14] S. S. Zhang, X. L. Yu, J. Ye, and W. M. Liu, Phys. Rev. A **87**, 063623 (2013).

[15] Fadi Sun, X.-L. Yu, J. Ye, H. Fan, and W.-M. Liu, Sci. Rep. **3**, 2119 (2013).

[16] Fadi Sun, Jinwu Ye, and Wu-Ming Liu, Phys. Rev. A **92**, 043609 (2015).

[17] Fadi Sun, Jinwu Ye, and Wu-Ming Liu, arXiv:1502.05338; Phys. Rev. B **94**, 024409 (2016).

[18] Fadi Sun, Jinwu Ye, and Wu-Ming Liu, arXiv:1601.01642.

[19] E. Stoner, Philos. Mag. **15**, 1018 (1933).

[20] J. A. Hertz, Phys. Rev. B **14**, 1165 (1976).

[21] A. J. Millis, Phys. Rev. B **48**, 7183 (1993); U. Zülicke and A. J. Millis, *ibid.* **51**, 8996 (1995).

[22] O. Zachar, S. A. Kivelson, and V. J. Emery, Phys. Rev. B **57**, 1422 (1998); For a review, see S. A. Kivelson *et al.*, Rev. Mod. Phys. **75**, 1201 (2003).

[23] Jinwu Ye, Nucl. Phys. B **805**, 418 (2008).

[24] G. B. Jo *et al.*, Science **325**, 1521 (2009).

[25] R. A. Duine and A. H. MacDonald, Phys. Rev. Lett. **95**, 230403 (2005); D. Pekker, M. Babadi, R. Sensarma, N. Zinner, L. Pollet, M. W. Zwierlein, and E. Demler, *ibid.* **106**, 050402 (2011); S. Pilati, G. Bertaina, S. Giorgini, and M. Troyer, *ibid.* **105**, 030405 (2010).

[26] C. Sanner, E. J. Su, A. Keshet, W. Huang, J. Gillen, R. Gommers, and W. Ketterle, Phys. Rev. Lett. **106**, 010402 (2011); **108**, 240404 (2012).

[27] Y. Shin, C. H. Schunck, A. Schirotzek, and W. Ketterle, Nature (London) **451**, 689 (2008).

[28] N. Gemelke, X. Zhang, C.-L. Huang, and C. Chin, Nature (London) **460**, 995 (2009).

[29] J. Kinast *et al.*, Science **307**, 1296 (2005); M. J. H. Ku *et al.*, *ibid.* **335**, 563 (2012).

[30] M. Kozuma, L. Deng, E. W. Hagley, J. Wen, R. Lutwak, K. Helmerson, S. L. Rolston, and W. D. Phillips, Phys. Rev. Lett. **82**, 871 (1999); J. Stenger *et al.*, *ibid.* **82**, 4569 (1999); D. M. Stamper-Kurn *et al.*, *ibid.* **83**, 2876 (1999); J. Steinhauer, R. Ozeri, N. Katz, and N. Davidson, *ibid.* **88**, 120407 (2002); S. B. Papp *et al.*, *ibid.* **101**, 135301 (2008); P. T. Ernst *et al.*, Nat. Phys. **6**, 56 (2010).

[31] Jinwu Ye *et al.*, Phys. Rev. A **83**, 051604(R) (2011); Ann. Phys. **328**, 103 (2013).

[32] Z.-F. Xu, L. You, and M. Ueda, Phys. Rev. A **87**, 063634 (2013).

[33] B. M. Anderson, G. Juzeliunas, V. M. Galitski, and I. B. Spielman, Phys. Rev. Lett. **108**, 235301 (2012).

[34] S. A. Brazovskii, Sov. Phys. JETP **41**, 85 (1975).

[35] P. M. Chaikin and T. C. Lubensky, *Principles of Condensed Matter Physics* (Cambridge University Press, Cambridge, England, 1995).

[36] Longhua Jiang and Jinwu Ye, Phys. Rev. B **76**, 184104 (2007). These authors show that for this kind of bosonic Lifshitz transition, the optimal lattice structure is a stripe. This is further confirmed by the RPA calculation here.

[37] For scaling functions across a topological fermionic Lifshitz transition, see [15].

[38] Jinwu Ye, Phys. Rev. Lett. **97**, 125302 (2006); Europhys. Lett. **82**, 16001 (2008); J. Low Temp. Phys. **160**, 71 (2010); Yu Chen, Jinwu Ye, and Quang Shan Tian, *ibid.* **169**, 149 (2012). Similarly to the superfluid-to-solid transition in ^{4}He, the first-order transition can happen before δ_{T-} reaches zero.

[39] Jinwu Ye and Longhua Jiang, Phys. Rev. Lett. **98**, 236802 (2007); Jinwu Ye, *ibid.* **97**, 236803 (2006); Ann. Phys. (NY) **323**, 580 (2008); J. Low Temp. Phys. **158**, 882 (2010).

[40] Leo Radzihovsky, Phys. Rev. A **84**, 023611 (2011).

[41] We also performed extensive numerical calculations of the collective modes inside the putative FM and find that they always become negative in some momentum regimes, indicating the instability of the putative FM state.

[42] Note that at the static limit $\omega = 0$, $\chi_{ij}(\vec{q},0)$ in Eq. (7) is real, so $\chi_{nL}(\vec{q},0) = 0$; there is no coupling between the density and longitudinal mode at the quadratic level. We also find $\chi_{nn}(Q_L,0)$ is finite, so the transition is *not* charge driven, in sharp contrast to the stripe charge ordering found in high-T_c superconductors [22].

[43] G. Gruner, Rev. Mod. Phys. **66**, 1 (1994).

[44] As shown in Fig. 2(b), at $\gamma = 0.82$, the system is in the SSDW phase. Here we draw the FS reconstruction in the LSDW+CDW phase for a comparison.

[45] Thomas Vojta, D. Belitz, R. Narayanan, and T. R. Kirkpatrick, Z. Phys. B **103**, 451 (1997).

[46] T. Senthil, Matthias Vojta, and Subir Sachdev, Phys. Rev. B **69**, 035111 (2004).

[47] Subir Sachdev, Phys. Rev. Lett. **105**, 151602 (2010).

[48] J. Ye and S. Sachdev, Phys. Rev. B **44**, 10173 (1991).

[49] Jinwu Ye, Phys. Rev. B **65**, 214505 (2002).

[50] For example, see M. C. Gutzwiller, Phys. Rev. Lett. **10**, 159 (1963); Phys. Rev. **137**, A1726 (1965); J. Kanamori, Prog. Theor. Phys. **30**, 275 (1963); Y. M. Vilk, L. Chen, and A.-M. S. Tremblay, Phys. Rev. B **49**, 13267 (1994); For a review, see A. Auerbach, *Interacting Electrons and Quantum Magnetism* (Springer-Verlag, New York, 1994).

[51] M. Trinker *et al.*, Appl. Phys. Lett. **92**, 254102 (2008).

[52] S. Sachdev, *Quantum Phase Transitions* (Cambridge University Press, Cambridge, 1999).